Available online at www.sciencedirect.com
ScienceDirect
International Journal of Heat and Mass Transfer 50 (2007) 1805–1822
International Journal of HEAT and MASS TRANSFER
www.elsevier.com/locate/ijhmt

Modelling of turbulent molten pool convection in laser welding of a copper–nickel dissimilar couple

Nilanjan Chakraborty [a,1], Suman Chakraborty [b,*]

[a] Department of Engineering, University of Liverpool, Brownlow Hill, Liverpool L69 3GH, UK
[b] Department of Mechanical Engineering, Indian Institute of Technology, Kharagpur 721302, West Bengal, India

Received 7 June 2006; received in revised form 29 September 2006
Available online 2 January 2007

Abstract

The effects of turbulence on momentum, heat, and mass transfer during laser welding of a copper–nickel dissimilar couple are studied by carrying out three-dimensional unsteady Reynolds Averaged Navier Stokes (RANS) simulations. The turbulent transport is modelled by a suitably modified high Reynolds number k–ε model. The solid–liquid phase change is accounted for by a modified enthalpy porosity technique. In order to demonstrate the effects of turbulence, two sets of simulations are carried out for the same set of processing parameters: one with the turbulence model, and the other without activating the turbulence model. The enhanced diffusive transport associated with turbulence is shown to decrease the maximum values of temperature, velocity magnitude, and copper mass fraction in the molten pool. The effects of turbulence are found to be most prominent on the species transport in the molten pool. The composition distribution in turbulent simulation is found to be more uniform than that obtained in the simulation without turbulent transport. The nickel composition distribution predictions, as obtained from the present turbulence model based simulations, are also found to be in good agreement with the corresponding experimental results.

Keywords: Turbulence; k–ε model; Diffusive transport; Heat; Momentum and mass transfer; Enhanced mixing

1. Introduction

Laser welding of dissimilar metal with disparate thermophysical properties offers some advantages over the traditional arc welding applications primarily due to the fact that laser processing is free of any beam-deflection effects otherwise associated with arc welding processes. However, in laser beam welding of dissimilar metals, the differences in physical properties of the materials lead to an asymmetry in the pertinent heat and fluid flow characteristics, as well as perceptible complexities in the solute segregation patterns. These, in turn, leave their imprints on the final welded microstructure. Therefore, a fundamental understanding of the molten pool transport in dissimilar metal welding is necessary in order to provide significant physical insights into the dynamic evolution of the constituent phases from an inhomogeneous melt. This eventually leads to a comprehensive understanding on the development of unique features in the welded microstructure.

Computational modelling of laser beam welding of dissimilar metals has been the subject of intensive research over the past few years. Early efforts in this regard have been based on two-dimensional heat and fluid flow models [1–3], which have more recently been extended to three dimensions [4,5]. However, in all these studies, the fluid flow in the molten pool was assumed to be laminar in nature. On the other hand, it is well established that for typical surface tension driven thermo-solutal convective flows, turbulence is likely to be triggered off when the surface tension Reynolds number becomes of the order of 100 or more [6–8]. Such observations have been rigorously verified

* Corresponding author. Tel.: +91 3222 282990; fax: +91 3222 282278.
E-mail addresses: n.chakraborty@liverpool.ac.uk (N. Chakraborty), suman@mech.iitkgp.ernet.in (S. Chakraborty).
[1] Tel.: +44 151 794 4831; fax: +44 151 794 4848.

0017-9310/$ - see front matter © 2006 Elsevier Ltd. All rights reserved.
doi:10.1016/j.ijheatmasstransfer.2006.10.030

Nomenclature

a_p, a_P^0	discretization equation coefficients
c	specific heat
C	species concentration
D	species mass diffusion coefficient
f_l	liquid fraction
g	acceleration due to gravity
h	convective heat transfer coefficient
k	turbulent kinetic energy
K	thermal conductivity
k_p	partition coefficient
L	latent heat of fusion
p	pressure
P	property
q	net power
q''	heat flux
Q	actual power input
r_q	radius of heat input
S	source term
T	temperature
t	time
u	x-component of velocity
U_{scan}	laser scanning speed
v	y-component of velocity
w	z-component of velocity
x, y, z	co-ordinates fixed to the laser source

Greek symbols

β_T	volumetric expansion coefficient of heat
β_C	volumetric expansion coefficient of solute
η	laser efficiency
μ_t	eddy viscosity
Γ	general diffusion term
ΔH	latent enthalpy
ε	turbulent kinetic energy dissipation rate
ε_r	emissivity
ϕ	general scalar variable
λ	relaxation factor
σ_{sur}	surface tension
σ_t	turbulent Prandtl number
σ_c	turbulent Schmidt number
σ_{rad}	Stefan–Boltzmann constant
ρ	density
μ	molecular viscosity

Superscript

$'$	stationary co-ordinate system

Subscripts

Cu (Ni)	copper (nickel)
max	maximum value
n	iteration level/normal direction
old	old iteration value
ref	reference
∞	ambient

through scaling analysis-based predictions [9], as well as by experimental observations [10] depicting strong surface oscillations in the molten pools formed during fusion welding operations. For typical high power laser material processing operations surface tension Reynolds numbers often becomes in the order of 1000 or more, where the concerned molten pool transport is expected to be turbulent in nature. Although a number of computational studies addressed turbulence modelling in case of joining of similar materials [11–16], the effects of turbulent transport on welding of dissimilar material pairs are yet to be reported. However, such studies can turn out to be of considerable practical importance, since they can provide significant physical insights into the fundamental understanding of the problem, along with an accurate description of the weld pool transport characteristics. This understanding, in turn, can effectively be used in order to predict micro-structural evolution in the dissimilar metal welding processes.

The aim of the present work is to develop a mathematical model for analyzing the role of turbulent transport features in the molten pool development during laser beam welding of dissimilar metals. In order to achieve this goal, a Reynolds Averaged Navier Stokes (RANS) equation based turbulent transport model developed by the present authors [14–18] for phase change material-processing applications is suitably extended to incorporate dissimilar metal welding features. Ideally, a Direct Numerical Simulation (DNS) would lead to the most accurate estimates of turbulence characteristics in the laser-molten pool. However, the computational cost of DNS scales as $Re_t^{11/4}$, where Re_t is the turbulent Reynolds number ($Re_t = \rho k^2/\varepsilon\mu$), which makes the proposition highly computationally prohibitive in nature. Moreover, the geometrical complexities associated with the morphological evolution of the molten pool make the problem almost intractable for DNS, within the constraints of current computational resources. It is expected that in the near future Large Eddy Simulation (LES) of the molten pool convection will be possible, which can potentially provide a significant amount of insight on the pertinent turbulent transport. However, with the present state of computational power, unsteady RANS simulations are probably the only economically feasible tools for analyzing such a complicated process of turbulent molten pool convection in laser joining of dissimilar metals. The turbulence model described in this work

is applied to a typical high power continuous dissimilar metal laser welding, for which turbulent convection effects are expected to be distinctly prominent. In order to demonstrate the unique features of turbulent convection in dissimilar welding applications, separate simulations are also carried out by employing the same set of processing parameters, but without activating the turbulence models. Based on these numerical simulation predictions, primary focus of the present investigation is directed towards achieving the following:

1. To characterize turbulent heat and mass transfer in a typical high power dissimilar metal welding process.
2. To demonstrate the effects of turbulence in the molten pool transport, in comparison to the predictions obtained without activating the turbulence modelling features.

In order to demonstrate the quantitative predictive capabilities of the present model, a binary system of Cu and Ni is chosen for the present study. Such a system is characterized with simple isomorphous phase diagrams without a miscibility gap or formation of inter-metallic compounds, which significantly simplifies the underlying mathematical analysis to a large extent. On the other hand, Cu and Ni have significant differences in thermo-physical properties, so that the fundamental physical issues associated with dissimilar metal welding processes can be aptly demonstrated. Further, experimental studies, as well as numerical computations based on laminar transport models for Cu–Ni dissimilar couple, are also well documented in the literature [4,5], which offers the convenience of a critical assessment of the prediction capabilities of the mathematical model developed in this study.

2. Mathematical modelling

A schematic diagram of a typical continuous laser welding of a binary couple is shown in Fig. 1. Two workpieces of Cu and Ni are kept side by side in a butt joint arrangement. According to Fig. 1, the laser torch moves in negative x direction along the line separating Cu and Ni blocks. A part of laser power only becomes available to the workpiece, which is specified by the laser coupling efficiency, η, as [19]

$$q = \eta Q \tag{1}$$

where q is the available power to the workpiece and Q is the total laser power. For dissimilar metal welding applications, a precise specification of this laser efficiency may be somewhat troublesome, since a better surface finish is found to reduce its value, whereas vapour and plasma formation tends to increase η [4]. Physical data available in this regard are not very adequate. In the present study, a laser coupling efficiency of 12% is employed, consistent with earlier numerical studies on laser-aided melting processes [17,18]. The material pair is heated to high temperatures within a very short period of time because of this incidence of a high-intensity laser beam. Once temperature of either of these two components rises beyond the corresponding melting point, a strong surface tension driven convection is likely to set in. This can give rise to strong intermixing between the constituent materials. The extent of this intermixing eventually gives rise to the final microstructure of the re-solidified component, which in turn governs mechanical properties.

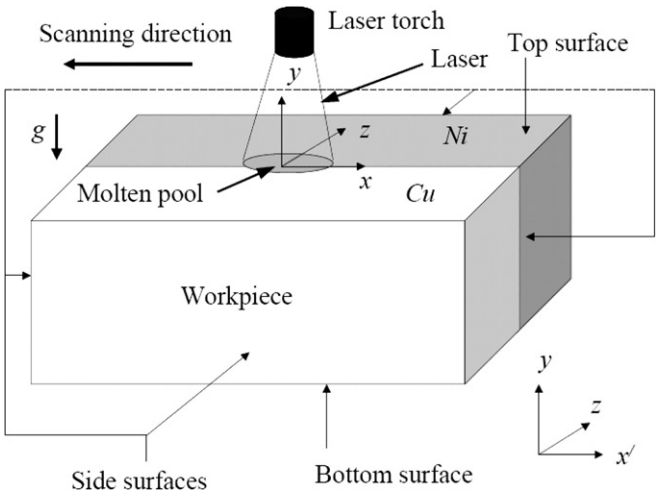

Fig. 1. Schematic diagram of laser welding of a Cu–Ni dissimilar couple.

From the above discussion, it becomes apparent that mathematical modelling of the melting and inter-mixing processes happens to be one of the key aspects in numerical simulation of dissimilar metal welding processes. In the literature, two different types of models, namely, the locally homogeneous mixture model and the multi-fluid model, have been commonly employed to address analogous physical situations. The locally homogeneous mixture model can be used under the assumption that the constituting species can mix up to the atomic level. In this situation, the mass transfer takes place purely by advection and diffusion processes. The multi-fluid model, on the other hand, addresses the situations in which different species are mixed over larger scales and can potentially have separate flow features [20,21]. The individual flow fields interact amongst themselves by some empirically specified inter-phase interaction terms. In the present study, a locally homogeneous mixture model is adopted, in which properties of the mixture are determined by relative proportions of the constituent components. Although some information related to characteristics of the mixture at the interface get eventually smeared out while employing this approach, the physical essence of the transport characteristics can still be reliably captured, as established in the earlier numerical studies on dissimilar metal welding processes [4]. For mathematical modelling, following simplifying assumptions are further invoked:

1. The molten metal flows for both Cu and Ni are assumed to Newtonian in nature.

2. The molten meal is incompressible, and thus the density change due to the temperature variations is taken care of by the Boussinesq's approximation.
3. Laser power is assumed to be distributed in a Gaussian manner at the top surface.
4. The top surface of the welded joint is assumed to statistically flat [4].
5. Thermo-physical properties are taken to be different for solid and liquid phases. The physical properties vary according to the concentration of individual components. Thermal conductivity, viscosity, specific heat, density and surface tension of the mixture at a given temperature are taken to be linear functions of constituent mass fractions.

The description of the governing conservative equations employed in this study rests on a single-domain continuum based enthalpy-porosity formulation [22]. In this methodology the transport equations for individual phases are volume-averaged to come up with a set of equivalent single-phase conservation equations, which are valid over the entire domain, irrespective of the constituent phases locally present. Based on the already solved thermal field the liquid fraction of a given control volume is evaluated, which implicitly specify and update the interfacial locations with respect to space and time. To achieve this purpose, dynamic evolution/absorption of latent heat is accounted for by a continuous updating of nodal latent enthalpy values in each computational cell, in accordance with the prevailing temperature field. This updating is reflected in the energy conservation equation, as either a heat source/sink. A distinctive advantage of this methodology is that no explicit conditions for energy conservation at the solid–liquid interface need to be accounted for. Moreover, since this approach does not need explicit interface tracking, it is well-suited for treating the continuous transitions between solid and liquid phases, as well as evolution of latent energy over a finite temperature range.

2.1. Governing equations

The governing differential equations described in the subsequent discussion are all transformed with reference to a co-ordinate system ($x_1 = x, x_2 = y, x_3 = z$) that translates with the laser source with a constant scanning speed, U_{scan}, along the negative x_1 direction. With this Galilean transformation of co-ordinates, the transport equations assume the following forms in Cartesian tensor notations. In all the equations, for each primitive variable ϕ, $\bar{\phi}$ represents the mean value and ϕ' represents the corresponding fluctuating component.

2.1.1. Conservation of mass

A statement of conservation of mass for fluid flow, in terms of the mean and fluctuating velocity components, can be written as

$$\frac{\partial \rho}{\partial t} + \frac{\partial(\rho \bar{u}_i)}{\partial x_i} = 0, \quad \frac{\partial(\rho u_i')}{\partial x_i} = 0 \tag{2}$$

2.1.2. Conservation of linear momentum

The single-phase Reynolds averaged Navier Stokes equation for the ith direction is given by ($i = 1, 2, 3$)

$$\begin{aligned}\frac{\partial(\rho \bar{u}_i)}{\partial t} &+ \frac{\partial(\rho \bar{u}_i \bar{u}_j)}{\partial x_j} \\ &= -\frac{\partial \bar{p}}{\partial x_i} + \rho g \delta_{i2} \beta_T (\overline{T} - T_{\text{ref}}) + \rho g \delta_{i2} \beta_C (\overline{C} - C_{\text{ref}}) \\ &\quad + \overline{S}_i + \frac{\partial}{\partial x_j}\left(\mu \frac{\partial \bar{u}_i}{\partial x_j} - \rho \overline{u_i' u_j'}\right) - U_{\text{scan}} \frac{\partial(\rho \bar{u}_i)}{\partial x_1}\end{aligned} \tag{3}$$

where g is the acceleration due to gravity, T_{ref} is taken to be equal to the melting temperature of the base material and C_{ref} is taken to be equal to the concentration of the alloying species at that reference temperature. The component of the source term $\overline{S}_i$ in Eq. (3) originates from the consideration that the morphology of the phase change domain can be treated as an equivalent porous medium that offers a resistance towards the fluid flow in that region. In a single-domain fixed-grid enthalpy-porosity formulation, this resistance can be conveniently formulated using Darcy's model, in association with the Cozeny–Karman relationship [22] as

$$\overline{S}_i = -\frac{K_{\text{m}}(1 - f_{\text{l}}^2)}{f_{\text{l}}^3 + b} \bar{u}_i \tag{4}$$

where f_{l} is the liquid fraction, given as $f_{\text{l}} = \Delta H / L$, with ΔH being the latent enthalpy content of a control volume and L being the latent heat of fusion. In Eq. (4), K_{m} is a morphological constant which depends on the morphology of the mushy region (i.e., dendritic arm spacing, etc.) [7]. The magnitude of K_{m} is typically a large number ($\sim 10^8$) [4,5,7,14–19,22] and b is a small number ($\sim 10^{-30}$) to avoid division by zero. The above formulation effectively ensures that the velocity undergoes a smooth transition from a zero value in solid region to a finite value in the fully liquid region. The details of formulation of the above term can be found in Brent et al. [22], and are not repeated here for the sake of brevity.

2.1.3. Conservation of energy

The single-phase thermal energy equation for turbulent flow is given by

$$\begin{aligned}\frac{\partial(\rho c \overline{T})}{\partial t} &+ \frac{\partial(\rho c \bar{u}_i \overline{T})}{\partial x_i} \\ &= \frac{\partial}{\partial x_i}\left(K \frac{\partial \overline{T}}{\partial x_i}\right) - \frac{\partial(\rho \Delta H)}{\partial t} - \frac{\partial}{\partial x_i}(\rho \bar{u}_i \Delta H) - \frac{\partial(\rho c \overline{u_i' T'})}{\partial x_i} \\ &\quad - U_{\text{scan}} \frac{\partial(\rho c \overline{T})}{\partial x_1} - U_{\text{scan}} \frac{\partial(\rho \Delta H)}{\partial x_1}\end{aligned} \tag{5}$$

where c is the specific heat of the material, K is the thermal conductivity, and ΔH is the latent enthalpy content of the

computational cell under consideration, which is constrained by the following expression:

$$\begin{aligned}\Delta H &= f(T) = L \quad \overline{T} > T_{\mathrm{l}} \\ &= f_{\mathrm{l}} L \quad T_{\mathrm{s}} \leqslant \overline{T} < T_{\mathrm{l}} \\ &= 0 \quad \overline{T} < T_{\mathrm{s}}\end{aligned} \tag{6}$$

where T_{s} and T_{l} are the solidus and liquidus temperatures, respectively which can be obtained from phase diagram for a given composition for general solid–liquid phase change. In the context of locally homogeneous mixing model the phase change is assumed to take at a temperature T_{ph}, and T_{s} and T_{l} are taken to be equal to T_{ph} [4,5]. The equivalent phase change temperature, T_{ph}, is assumed to be a linear function of composition, in the following form [4]:

$$T_{\mathrm{ph}} = (T_{\mathrm{melt}})_{\mathrm{Cu}}\overline{C} + (T_{\mathrm{melt}})_{\mathrm{Ni}}(1-\overline{C}) \tag{7}$$

where $(T_{\mathrm{melt}})_i$ is the melting point temperature of the constituent 'i' forming the mixture. The latent heat of fusion, L, for a given control volume is assumed to be given by a linear combination of latent heats of fusion for pure Cu and Ni, following Phanikumar et al. [4]

$$L = L_{\mathrm{Cu}}C + L_{\mathrm{Ni}}(1-C) \tag{8}$$

where L_{Cu} and L_{Ni} are latent heats of fusion for pure Cu and Ni, respectively, and C is the mass fraction of Cu at the given control volume.

2.1.4. Species conservation

The species conservation equation is given by

$$\frac{\partial(\rho\overline{C})}{\partial t} + \frac{\partial(\rho\bar{u}_i\overline{C})}{\partial x_i} = \frac{\partial}{\partial x_i}\left(\rho D\frac{\partial\overline{C}}{\partial x_i}\right) - \frac{\partial(\rho\overline{u_i'C'})}{\partial x_i} - U_{\mathrm{scan}}\frac{\partial(\rho\overline{C})}{\partial x_1} \tag{9}$$

where D represents the binary mass diffusivity of the Cu–Ni couple.

2.1.5. Modelling of Reynolds stress ($-\rho\overline{u_i'u_j'}$)

In the present analysis, the Reynolds stress $-\rho\overline{u_i'u_j'}$, appearing in Eq. (3), are modelled by a gradient hypothesis of the form

$$-\rho\overline{u_i'u_j'} = \mu_{\mathrm{t}}\left(\frac{\partial\bar{u}_i}{\partial x_j} + \frac{\partial\bar{u}_j}{\partial x_i}\right) - \frac{2}{3}\delta_{ij}\rho k \tag{10}$$

Here, the eddy viscosity, μ_{t}, is given by

$$\mu_{\mathrm{t}} = \sqrt{f_{\mathrm{l}}}C_\mu\rho k^2/\varepsilon \tag{11}$$

where k and ε are turbulent kinetic energy and the dissipation rate of turbulent kinetic energy, respectively. The quantities k and ε are evaluated by solving two modelled additional closure transport equations. In Eq. (11), C_μ is a model constant, which is taken to be 0.09 [23]. It is important to note that in a standard high Reynolds number $k-\varepsilon$ model, the factor $\sqrt{f_{\mathrm{l}}}$ does not appear in the eddy viscosity expression. In the present problem, one encounters both solid and liquid phases in the computational domain. As a result, the mathematical formulation should ensure an asymptotically smooth reduction of eddy viscosity, eddy thermal conductivity and eddy mass diffusion coefficients (altogether, in a generalized term, eddy diffusivity) to their respective molecular values, as one proceeds from the bulk liquid region to the liquidus interface of the phase-changing front. In order to satisfy these requirements, Shyy et al. [8] used a modified eddy viscosity expression for modelling solid–liquid phase transition problems by introducing a damping factor $\sqrt{f_{\mathrm{l}}}$, which is followed in the present study as well.

2.1.6. Modelling of turbulent heat fluxes ($-\rho c\overline{u_i'T'}$)

Following the same analogy as the Reynolds stresses, the turbulent heat fluxes (Reynolds heat fluxes) appearing in Eq. (6) are given by the following expression, according to gradient transport hypothesis:

$$-\overline{u_i'T'} = \alpha_{\mathrm{t}}\partial\overline{T}/\partial x_i \tag{12}$$

where α_{t} is the eddy thermal diffusivity. From the analogy of laminar flow, α_{t} can be expressed as

$$\alpha_{\mathrm{t}} = \mu_{\mathrm{t}}/\rho\sigma_{\mathrm{t}} \tag{13}$$

where σ_{t} is the turbulent Prandtl number. In the present case, σ_{t} is taken to be 0.9.

2.1.7. Modelling of turbulent mass fluxes ($-\rho\overline{u_i'C'}$)

Following the same analogy as the Reynolds heat fluxes, the turbulent mass fluxes (Reynolds mass fluxes) appearing in Eq. (9) are modelled as

$$-\overline{u_i'C'} = \alpha_c\partial\overline{C}/\partial x_i \tag{14}$$

where α_c is the eddy mass diffusivity. From the analogy of laminar flow, α_c can be expressed as

$$\alpha_c = \mu_{\mathrm{t}}/\rho\sigma_c \tag{15}$$

where σ_c is turbulent Schmidt number. It has been proposed that σ_c varies from 0.8 to 0.9 [23]. In the present work, σ_c is taken to be 0.9.

2.1.8. Governing equations for k and ε

The modelled governing equations for k and ε, as applicable in the present context, are given by

$$\begin{aligned}\frac{\partial(\rho k)}{\partial t} + \rho\bar{u}_j\frac{\partial k}{\partial x_j} = {} & \frac{\partial}{\partial x_j}\left[\left(\mu + \frac{\mu_{\mathrm{t}}}{\sigma_k}\right)\frac{\partial k}{\partial x_j}\right] \\ & + \mu_{\mathrm{t}}\left(\frac{\partial\bar{u}_i}{\partial x_j} + \frac{\partial\bar{u}_j}{\partial x_i}\right)\frac{\partial\bar{u}_i}{\partial x_j} - \frac{\mu_{\mathrm{t}}}{\sigma_{\mathrm{t}}}g\beta_T\frac{\partial\overline{T}}{\partial x_2} \\ & - \frac{\mu_{\mathrm{t}}}{\sigma_c}g\beta_C\frac{\partial\overline{C}}{\partial x_2} - \rho\varepsilon - \rho U_{\mathrm{scan}}\frac{\partial k}{\partial x_1}\end{aligned} \tag{16}$$

$$\frac{\partial(\rho\varepsilon)}{\partial t}+\rho\bar{u}_j\frac{\partial\varepsilon}{\partial x_j}=\frac{\partial}{\partial x_j}\left[\left(\mu+\frac{\mu_t}{\sigma_\varepsilon}\right)\frac{\partial\varepsilon}{\partial x_j}\right]+C_{\varepsilon1}\mu_t\left(\frac{\partial\bar{u}_i}{\partial x_j}+\frac{\partial\bar{u}_j}{\partial x_i}\right)\frac{\partial\bar{u}_i}{\partial x_j}\frac{\varepsilon}{k}-C_{\varepsilon1}\frac{\mu_t}{\sigma_k}g\beta_T\frac{\partial\overline{T}}{\partial x_2}\frac{\varepsilon}{k}-C_{\varepsilon1}\frac{\mu_t}{\sigma_c}g\beta_c\frac{\partial\overline{C}}{\partial x_2}\frac{\varepsilon}{k}-C_{\varepsilon2}\rho\frac{\varepsilon^2}{k}-\rho U_{\text{scan}}\frac{\partial\varepsilon}{\partial x_1} \quad (17)$$

Here, the different model constants are taken as follows:

$$\sigma_k=1.0,\quad \sigma_\varepsilon=1.3,\quad C_\mu=0.09,\quad C_{\varepsilon1}=1.44 \text{ and } C_{\varepsilon2}=1.92 \quad (18)$$

2.2. Boundary conditions

The boundary conditions for the primitive variables, with reference to the work piece (see Fig. 1), are given as follows:

2.2.1. Heat transfer and fluid flow boundary conditions

Considering Gaussian heat input, convective and radiation losses, the top surface thermal boundary condition can be written as

$$-K\partial\overline{T}/\partial y=-q''(r)+h(\overline{T}-T_\alpha)+\varepsilon_r\sigma_{\text{rad}}(\overline{T}^4-T_\alpha^4) \quad (19)$$

where $q''(r)$ is the net laser heat flux distributed in a Gaussian manner, with a radius of r_q. The heat transfer coefficient h and surface emissivity ε_r are taken to be 15.0 W/m^2 K and 0.8 respectively, following previous studies [4,5,14–19]. Further, since the top surface is assumed to be statistically flat [4], one can write

$$\overline{v}=0 \quad (20)$$

From the free surface shear balance between viscous forces and surface tension effects, one obtains

$$\tau_{12}=\mu\frac{\partial\bar{u}_1}{\partial x_2}=\frac{\partial\sigma_{\text{sur}}}{\partial x_1};\quad \tau_{13}=\mu\frac{\partial\bar{u}_3}{\partial x_2}=\frac{\partial\sigma_{\text{sur}}}{\partial x_3} \quad (21)$$

where σ_{sur} is the surface tension coefficient at the top (free) surface, which is taken to be as linear combination of surface tension coefficients of Cu and Ni, based on their respective mass fractions, as

$$\sigma_{\text{sur}}=(\sigma_{\text{sur}})_{\text{Cu}}\overline{C}+(\sigma_{\text{sur}})_{\text{Ni}}(1-\overline{C}) \quad (22)$$

Regarding the transport of k and ε, the free surface boundary conditions can be written as [7]

$$\partial k/\partial y=0,\quad \partial\varepsilon/\partial y=0 \quad (23)$$

The four side faces are subjected to the following convective heat transfer boundary condition [14–18]:

$$-K\partial\overline{T}/\partial n=h(\overline{T}_{\text{wall}}-T_\alpha) \quad (24)$$

where $\overline{T}_{\text{wall}}$ is the wall temperature, n is the direction of outward normal to the surface concerned and h is the convective heat transfer coefficient given by 10.0 W/m^2 K [4,5,14–19]. In the present study the domain size is taken in such a manner that the bottom surface remains sufficiently away from the molten pool. As a result, the boundary condition at bottom surface does not have significant influence on molten pool convection. Following earlier studies [4,5,14–19] the bottom face is assumed to be insulated, which implies

$$\partial\overline{T}/\partial y=0 \quad (25)$$

2.2.2. Mass transfer boundary conditions

In the absence of any net mass flux at the top surface, one may write

$$\partial\overline{C}/\partial y=0 \quad (26)$$

It should be noted here that the two constituent elements forming the workpiece can mix with each other indefinitely in the bulk liquid and the bulk solid phases. However, at the solidification interface, only a part of solute, namely $k_p\overline{C}$, goes into the solid phase (where k_p is the partition coefficient, given by $k_p=C_s/C_l$, C_s and C_l being the solid and liquid phase concentrations, as dictated based by the corresponding binary phase diagram, at a given temperature). Thus, the solute flux balance at the solidification front is given by [24]

$$-D\partial\overline{C}/\partial n=v_n\overline{C}(1-k_p) \quad (27)$$

where n is the direction of the outward normal to the interface, and v_n is the interfacial velocity in that direction. Likewise, the boundary condition at the fusion front can be written as [24]

$$-D\partial\overline{C}/\partial n=v_n\overline{C} \quad (28)$$

2.2.3. k–ε transport at near wall regions

In the context of k and ε transport, solid–liquid interfaces are treated as solid walls. For high Reynolds number k–ε model, eddy viscosity, eddy thermal diffusivity, and eddy mass diffusivity are specified at the grid points next to solid/liquid interface with the help of wall functions [23]. The wall functions prescribe the turbulence and mean velocity profiles in the regions close to the wall, where the mean velocity gradient, turbulent kinetic energy and its dissipation rate are given by

$$\frac{\partial\bar{u}_w}{\partial y}=\frac{u_\tau}{\kappa y_P};\quad \varepsilon=\frac{u_\tau^3}{\kappa y_P},\quad u_\tau=\sqrt{\frac{|\tau_w|}{\rho}}=C_\mu^{1/4}\sqrt{k} \text{ and } \mu_{\text{eff}}=\mu+\mu_t=\frac{\kappa\mu y_P^+}{\ln(9y_P^+)} \quad (29a)$$

where $y_P^+=\rho u_\tau y_P/\mu$, $\bar{u}_w$ is the mean velocity component at the near wall grid point tangential to the solid–liquid interface, y_P is normal distance of the grid point next to the solid–liquid interface (which is treated to be the wall), τ_w is the wall shear stress and κ is the Von Karman's constant ($\kappa=0.4$). The effective thermal and solutal diffusivities at

near wall points are also prescribed with the help of wall function according to Kader [25]:

$$\frac{K}{c}+\frac{\mu_t}{\sigma_t}=\frac{\mu y_P^+}{[\sigma_t(1/\kappa)\log(y_P^+)+(3.85Pr^{1/3}-1.3)^2+2.12\log(Pr)]} \tag{29b}$$

and

$$\rho D+\frac{\mu_t}{\sigma_c}=\frac{\mu y_P^+}{[\sigma_c(1/\kappa)\log(y_P^+)+(3.85Sc^{1/3}-1.3)^2+2.12\log(Sc)]} \tag{29c}$$

where Pr and σ_t are the molecular and turbulent Prandtl numbers, respectively, while Sc and σ_c are the molecular and turbulent Schmidt numbers, respectively. Furthermore, the conditions $k=0$ and $\partial\varepsilon/\partial n$ are used to specify k and ε at the solid–liquid interface. The values of k and ε come out identically zero in the solid phase according to the present solution procedure.

3. Numerical procedure

3.1. Overall solution scheme

The coupled conservation equations are iteratively solved using a pressure-based finite volume method according to the SIMPLER algorithm [26]. The convection–diffusion terms in the governing equations are discretised using a Power Law scheme [26]. The time advancement of both the convective and diffusive terms is carried out in a fully implicit manner. The system of linear algebraic equations is iteratively solved using a line-by-line Tri-Diagonal Matrix Algorithm (TDMA) solver [26]. The phase change aspects of the problem are numerically taken care of by an enthalpy porosity technique. The updating of latent enthalpy content of each computational cell is carried out according to the following expression [22]:

$$[\Delta H]_{n+1}=[\Delta H]_n+(a_P/a_P^0)\lambda c\{[T_P]_n-T_{ph}\} \tag{30}$$

where n is the iteration level, a_P and a_P^0 are the nodal point coefficient and coefficient associated with the transient part of discretised energy equation and λ is a relaxation factor.

3.2. Numerical implementation

The physical property values used in the computation are listed in Table 1 [27]. For a mixture, properties such as thermal conductivity (K), specific heat (c) or viscosity (μ) are calculated by using the following relation:

$$P=P_{Cu}\overline{C}+P_{Ni}(1-\overline{C}) \tag{31}$$

where P stands for K, c or μ, as the case may be, and the subscripts Cu and Ni stand for copper and nickel, respectively. The calculations for equivalent mixture properties are carried out at each time step after solving the species conservation equation. The results presented in this paper correspond to process parameters typical to dissimilar metal laser welding operations ($U_{scan}=0.008$ m/s, $Q=3.5$ kW, $\eta=0.12$, $r_q=0.5$ mm).

Table 1
List of physical properties

Physical properties	Values
β_T (compressibility)	0.45×10^{-4} K^{-1}
β_C (compressibility)	11.0×10^{-2}
T_m (melting point)	1085 °C (Cu)
	1453 °C (Ni)
L (latent heat)	1.88×10^5 J/kg (Cu)
	2.90×10^5 J/kg (Ni)
ρ (density)	8900 kg/m^3 (Cu)
	7900 kg/m^3 (Ni)
D (mass diffusivity Cu in Ni in liquid phase)	1×10^{-9} m^2/s[a]
σ_{sur} (surface tension)	$1.285–1.3\times10^{-4}(T-T_m)$ N/m (Cu)
	$1.778–3.4\times10^{-4}(T-T_m)$ N/m (Ni)
T_{ref} (reference temperature)	1085 °C
C_{ref} (reference composition)	0.0
μ (viscosity)	2.85×10^{-3} Pa s (Cu)
	3.68×10^{-3} Pa s (Ni)
K (thermal conductivity for Cu)	
Solid phase	279.5 W/m K
Liquid phase	170.7 W/m K
K (thermal conductivity for Ni)	
Solid phase	75.0 W/m K
Liquid phase	62.0 W/m K
c (specific heat for Cu)	
Solid phase	440.0 J/kg K
Liquid phase	484.0 J/kg K
c (specific heat for Ni)	
Solid phase	515.0 J/kg K
Liquid phase	595.0 J/kg K

[a] Mass diffusivity in liquid phase is taken in consultation with the website of Prof. H. K. Bhadeshia, Cambridge University, UK.

3.3. Choice of grid size

For the numerical simulations, it is necessary to adequately resolve the boundary layer formed just underneath the top surface of the molten pool, due to the strong thermo-solutal surface tension gradients prevailing in the shear layer. In turn, an appropriate resolution of boundary layer ensures an accurate estimation of the velocity gradients existing within the boundary layer. This further leads to an accurate evaluation of turbulent kinetic energy generation term in k equation. It is also necessary to have a threshold grid resolution adjacent to the solid–liquid interface so that the computational mesh distribution satisfies the requirements of a typical high Reynolds number k–ε model. Accordingly, the following criteria for the choice of grid size are effectively adopted.

3.3.1. Criterion-1

In order to adequately resolve the velocity boundary layer thickness (δ_v) at the top surface, it is important to have an estimate of δ_v in order to generate the computational

grid. The above boundary layer thickness is estimated by the following scaling relationship [28]:

$$\mu \frac{U_s}{\delta_v} \sim \left| \frac{\partial \sigma_{sur}}{\partial T} \right| \frac{\Delta T}{R} \tag{32}$$

where U_s is the surface velocity scale, and $\Delta T/R$ is the thermal gradient scale. In the above expression, R is the maximum width of the molten pool and ΔT is the difference between the pool temperature just beneath the laser source and the melting temperature of the concerned material. With typical thermo-physical properties listed in Table 1 and a value of U_s of the order of 1 m/s [4], δ_v turns out to be about 0.01 mm. Accordingly, a few (typically five) grid points are accommodated within that length, so as to capture strong velocity gradients in the surface tension driven boundary layer. Moreover, this resolution also ensures that the velocity gradients are evaluated with sufficient accuracy for the measurement of turbulent kinetic energy generation.

3.3.2. Criterion-2

The turbulent diffusivities for the grid points next to the wall are specified with the help of appropriate wall functions [23], in the context of a high Reynolds number k–ε model. To specify the diffusion coefficients near the wall using wall conditions, it is necessary to ensure that the grid points immediately next to the wall belong to the logarithmic layer. According to the original version of high Reynolds number k–ε model this condition is given by

$$x^+ > 40 \tag{33a}$$

$$\text{where} \quad x^+ = \rho C_\mu^{0.25} k^{0.5} \Delta x / \mu \tag{33b}$$

where Δx is the near-wall characteristic grid spacing in the wall-normal direction. However, in order to predict the wall heat flux satisfactorily it is necessary to have a finer grid. Accordingly, in the present study, the grid size is kept within a limit such that the near wall point falls inside either the buffer layer or the logarithmic layer. This condition is mathematically given by $20 < x^+ \leqslant 50$. The above requirement can be met by ensuring that the x^+ remains within 50, even for the maximum possible value of k. However, it unnecessarily entails too fine a grid resolution, which can increase the computational costs considerably. A trade-off between these two conflicting requirements, in practice, is best found by numerical trials and errors.

From these two major criteria indicated above, it is evident that the grid spacing in y direction is principally governed by criterion 1, and the grid distribution in the x and z directions is determined by criterion 2. Accordingly, a grid size of 2.42×10^{-6} m is chosen for the topmost grids. A grid spacing of 4.8×10^{-6} m is chosen for three grid points immediately beneath the topmost layer. This is followed by a grid size of 7.2×10^{-6} m, and subsequently, a grid size of 9.6×10^{-6} m over six consecutive grid spacings, which is followed by grid sizes of 1.2×10^{-5} m and 1.45×10^{-5} m, respectively, in the negative y direction. Thereafter, a uniform grid spacing of 2.42×10^{-5} m is employed for the remaining part of the pool. Outside the molten pool, a non-uniform coarser grid is chosen. In the x and z directions, an optimised grid size near the solid–liquid interface is found to be 6.43×10^{-5} m, after which the grid size is increased gradually to 1.34×10^{-4} m away from the molten zone. Overall, a $69 \times 48 \times 69$ grid system is used to discretise the working domain of size $x = 8$ mm $\times$ $y = 5$ mm $\times$ $z = 8$ mm. A comprehensive grid independence study reveals that the above choice of grid spacings turns out to be a reasonable optimisation from the point of view of numerical accuracy and computational economy. For the present study, the laser torch is assumed to be located at $x = 4$ mm, $y = 5$ mm, and $z = 3.94$ mm with respect to the moving co-ordinate system. The part of the working domain given by $z \leqslant 3.94$ mm is taken to be Cu workpiece and the part given by $z \geqslant 3.94$ mm is taken to be Ni workpiece. The x–y plane at $z = 3.94$ mm corresponds to the contact surface between Cu and Ni workpieces in the present study.

3.4. Choice of time step

For the present problem parameters, initiation of melting takes about 0.6 ms. Before the initiation of melting, the heat transfer takes place in conduction mode, during which a relatively larger time step (about 0.2 ms) is chosen, so that the melting point of Ni is reached within three time steps. However, with the start of melting, the high temperature gradient in the pool sets up a strong Marangoni (surface tension-driven) flow, leading to a convection-dominated transport. As, in this phase, convection in the molten pool develops rapidly, the solution is highly sensitive to the time step chosen. It is observed that a time step size only as small as about 0.05 ms can lead towards monotonic convergence of the solution during this period of initial transience. Typically, after about 5 ms, the molten pool reaches a state, when changes in dependent variables between the consecutive time steps are relatively small. At this stage, slightly larger time steps (typically about 0.7 ms) can safely be used to save the computational time. After 10 ms, the pool becomes sufficiently developed, which allows time steps as high as 0.001 s, without any numerical oscillations. Finally, the simulation is carried out up to 25 ms, which is typically the time associated with melting phase in dissimilar metal laser welding operations [4].

3.5. Convergence criteria

The convergence for all the dependent variable $(\bar{u}, \bar{v}, \bar{w}, \overline{T}, \overline{C}, k, \varepsilon)$ is checked after each iteration, within a given time step. Convergence at each grid point is assessed on the basis of relative errors, as given by the following criterion:

$$\left| \frac{\phi - \phi_{old}}{\phi_{max}} \right| \leqslant 10^{-4} \tag{34}$$

where ϕ is the value of a general scalar variable at a particular grid point at the current iteration level, ϕ_{old} is the value of the concerned variable at the same grid point at the previous iteration level, and ϕ_{max} is the maximum absolute value of the same over the entire domain.

4. Results and discussion

In the present study, two sets of simulations have been carried out for the same set of process parameters. In one set of simulations, the turbulence modelling is activated when the value of $Re = 2\rho U_{max} r_q/\mu$ exceeds 600, as per the criterion established by Atthey [6]. In the other set, the simulations are carried out without activating the turbulence models. These simulations with and without turbulence modelling will henceforth be referred to as the turbulent and laminar simulations respectively. Temperature, velocity, and species conservation fields, as obtained from these two sets of simulations, will be compared in order to demonstrate the effects of turbulence in dissimilar metal laser welding processes.

The isotherms on the top (free) surface, as obtained from laminar and turbulent simulations, are presented in Fig. 2a and b, respectively. One important observation is that the maximum temperature location is shifted towards the nickel side, which is consistent with the observations made by Phanikumar et al. [4]. The thermal diffusivity of Cu, being substantially higher than that of Ni, leads to a more rapid temperature rise in Ni than in Cu, in the conduction-dominated regime of the melting process. Although the melting point of Ni is higher than that of Cu, melting occurs much faster in case of Ni, due to its relatively lower thermal diffusivity. A combined consequence of the differences in thermal diffusivities of Cu and Ni and their melting at different times eventually affect the advective transport in the molten pool in a rather complicated manner. Although the temperature distributions within the melt-pool are qualitatively similar for both laminar and turbulent transport models (see Fig. 2a and b), significant quantitative differences in this regard may be noted. In particular, the maximum mean temperature in a turbulent pool turns out to be smaller than that in case of a laminar pool, as evident from Fig. 2a and b. This is because of the enhanced mixing effects associated with turbulent transport which augments the overall rate of thermal energy exchange in the molten pool leading to a lower peak temperature. This observation is found to be consistent with the previous findings on other surface melting operations [14–18]. Comparing Fig. 2a and b, it is evident that the isotherms near the maximum temperature location in the case of laminar simulation are somewhat tilted towards copper side of the molten pool, whereas this effect is less prominent in the case of isotherms in turbulent simulation. This effect is principally due to the difference in the variation of thermal diffusivity induced by the different solute concentration distribution between the laminar and turbulent molten pool. In order to understand this behaviour, it

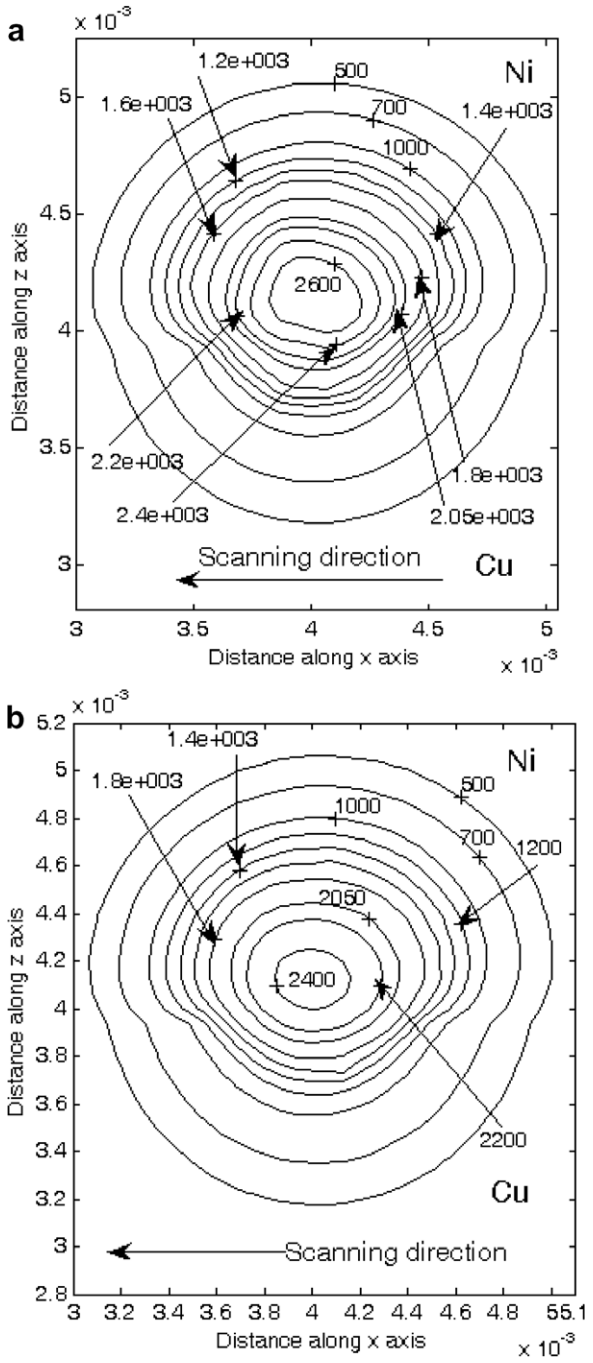

Fig. 2. Isotherms in the top surface after 25 ms from (a) laminar simulation, (b) turbulent simulation. All the temperatures are shown in °C. In the contour labels, 1e+3 indicates 1000 units. In moving coordinate system laser torch located at $x = 4$ mm, and $z = 3.94$ mm. At time $t = 0$ s, $z = 3.94$ mm indicates the separation line between Cu and Ni workpieces.

is instructive to examine the copper concentration fields shown in Fig. 3a and b, where the distinctive features of turbulent species transport can be clearly identified. In both laminar and turbulent cases, freshly molten Cu gets transported towards the Ni side of the molten pool, by combined advection–diffusion mechanisms. In the Ni rich side of the molten pool, the Cu concentration is diluted

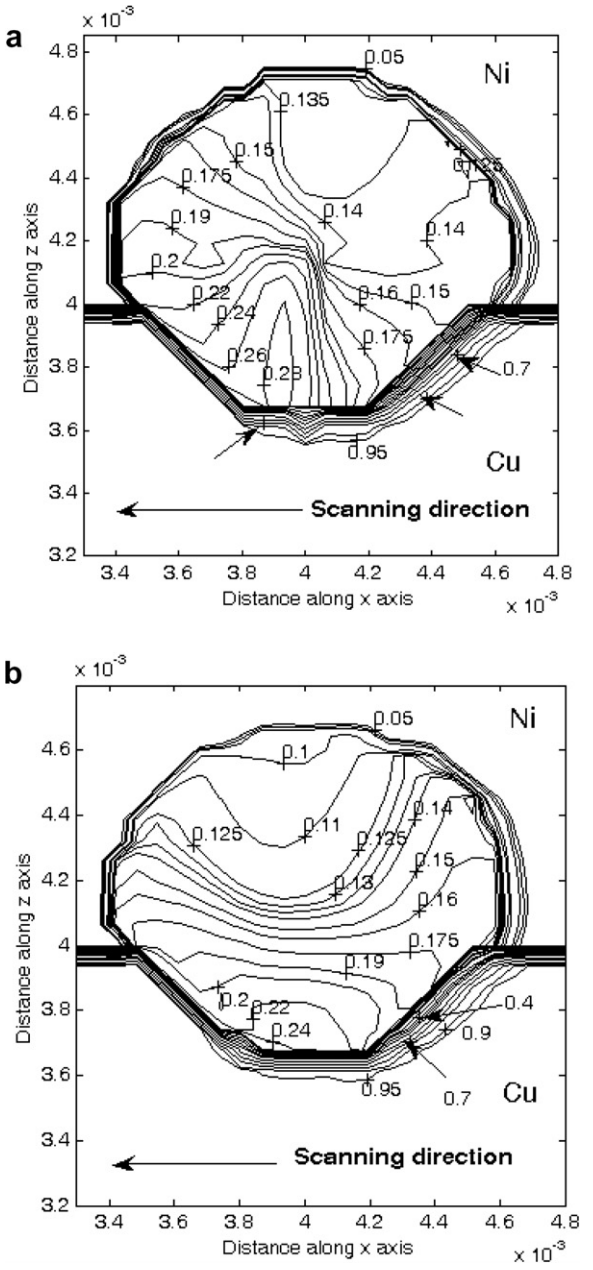

Fig. 3. Cu mass fraction contours in the top surface after 25 ms from (a) laminar simulation, (b) turbulent simulation. In moving co-ordinate system laser torch located at $x = 4$ mm, and $z = 3.94$ mm. At time $t = 0$ s, $z = 3.94$ mm indicates the separation line between Cu and Ni workpieces.

by a fresh addition of molten Ni. A preferential rejection of Cu takes place in the solidification front of the Ni rich side, which locally increases the Cu concentration. With diffusive mixing effects being more prominent in case of turbulent transport, the consequent solute distribution effects give rise to a more distinct "banded" structure in the Cu concentration field, as compared to that in a laminar molten pool. It should be noted from Fig. 3 that the concentration contours are crowded along the joint plane outside the molten pool, which is purely an artefact of the interpolation routines that are commonly employed for post processing of the output data in the vicinity of discontinuous phase boundaries [4,5], and should not be associated with any physical meaning. This is also applicable to the other concentration contours presented in the following discussion.

Regarding the combined thermo-solutal contributions to the velocity field, it can be noted that the surface tension gradients ($\partial\sigma_{sur}/\partial x$ and $\partial\sigma_{sur}/\partial z$) at the top surface initiate the convective transport in the molten pool. These surface tension gradients, in turn, are determined by both the temperature and concentration gradients, as

$$\frac{\partial\sigma_{sur}}{\partial x} = \frac{\partial\sigma_{sur}}{\partial T}\frac{\partial\overline{T}}{\partial x} + \frac{\partial\sigma_{sur}}{\partial C}\frac{\partial\overline{C}}{\partial x} \quad \text{and}$$
$$\frac{\partial\sigma_{sur}}{\partial z} = \frac{\partial\sigma_{sur}}{\partial T}\frac{\partial\overline{T}}{\partial z} + \frac{\partial\sigma_{sur}}{\partial C}\frac{\partial\overline{C}}{\partial z} \tag{35a}$$

The surface tension gradients of temperature and concentration, namely, $\partial\sigma_{sur}/\partial T$ and $\partial\sigma_{sur}/\partial C$, respectively, are given by

$$\frac{\partial\sigma_{sur}}{\partial T} = \left(\frac{\partial\sigma_{sur}}{\partial T}\right)_{Cu}\overline{C} + \left(\frac{\partial\sigma_{sur}}{\partial T}\right)_{Ni}(1-\overline{C}) \quad \text{and}$$
$$\frac{\partial\sigma_{sur}}{\partial C} = (\sigma_{sur})_{Cu} - (\sigma_{sur})_{Ni} \tag{35b}$$

For Cu–Ni mixture, $\frac{\partial\sigma_{sur}}{\partial T}$ and $\frac{\partial\sigma_{sur}}{\partial C}$ are negative in nature. Therefore these two effects essentially oppose each other, where the temperature and concentration gradients are of opposite sign. The resultant effect, as dictated by the ratio of the quantities $|\frac{\partial\sigma_{sur}}{\partial T}\frac{\partial\overline{T}}{\partial x_i}|$ and $|\frac{\partial\sigma_{sur}}{\partial C}\frac{\partial\overline{C}}{\partial x_i}|$ $(i = 1, 3)$, depends on the relative strength of the thermal or solutal gradients of surface tension. From the velocity vector plots depicted in Fig. 4a and b, it is evident that for both laminar and turbulent simulations, thermally induced gradients in surface tension dominate over the solutal gradients of surface tension. However, in case of turbulent transport, the mean thermal and concentration gradients decrease due to the increased diffusion strength. This eventually decreases the strength of Marangoni convection in turbulent pool. Moreover, a greater degree of momentum diffusion in the turbulent pool results in a decrease in the maximum velocity magnitude, as evident from Fig. 4a and b. As a result, in the case of turbulent transport, the mean advection of heat from the centre of the pool towards its peripheries is weaker than that in the case of laminar transport, which tends to decrease the pool width. On the other hand, an enhanced diffusive transport of thermal energy tends to widen the turbulent molten pool. The relative strength of these two counteracting mechanisms, in presence of turbulent transport, ultimately determines the final weld pool shape. Comparing Fig. 3a and b, it can be observed that for the present case study, the laminar weld pool appears to be slightly wider than the corresponding turbulent pool.

It is apparent from Fig. 3a and b that Cu is transported towards the Ni side from the centre of the pool due to radially outward fluid motion. However, the iso-concentration

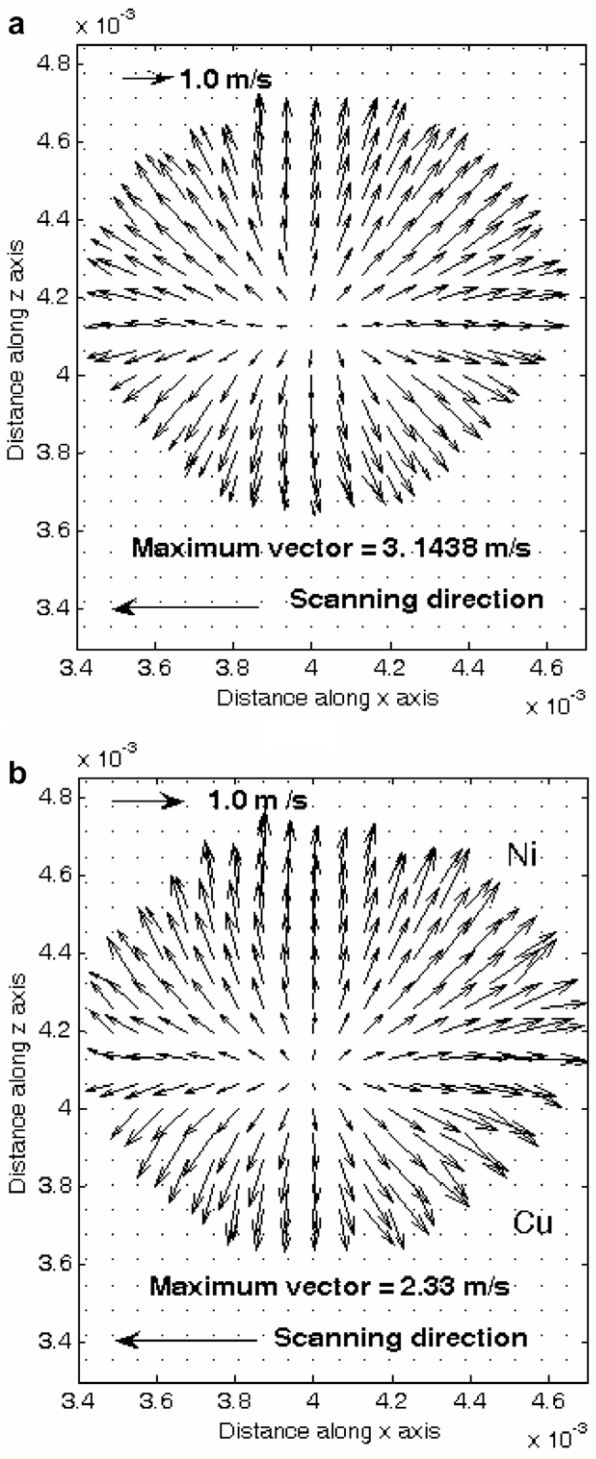

Fig. 4. Top surface velocity vector in the molten pool after 25 ms: (a) laminar simulation, (b) turbulent simulation. In moving co-ordinate system laser torch located at $x = 4$ mm, and $z = 3.94$ mm. At time $t = 0$ s, $z = 3.94$ mm indicates the separation line between Cu and Ni workpieces.

contours of Cu near the solid–liquid interface in the Ni rich side of the molten pool show convex curvature towards the centre of the pool. This is because of the addition of fresh Ni in the molten pool due to melting, which in turn sets up a concentration gradient and diffuses towards the centre of the molten pool. If the diffusive transport of fresh Ni towards the pool centre overcomes the advection of Cu, then the concentration of copper gets diluted the near the solid–liquid interface towards the Ni side and the iso-concentration contours of Cu show a convex curvature towards the centre of the pool. This effect is present in both laminar and turbulent pools, and is consistent with earlier laminar simulations of Phanikumar et al. [5]. The above-mentioned convex curvature of Cu iso-concentration contours is more prominent in a turbulent weld pool, since the diffusion of Ni from the melting front becomes stronger and the mean advective transport of Cu becomes weaker in turbulent transport.

Regarding the morphology of a dynamic evolution of the molten pool, it can be noted that the fluid flow emanating from the hottest part of the pool also transports heat in the longitudinal and side-wise directions. The fluid stream encountering a solid–liquid interface takes a turn in the downward direction, thereby giving rise to a toroidal circulation pattern in the molten pool, as apparent from Fig. 5 for both laminar and turbulent simulations. The corresponding temperature and Cu composition contours in the longitudinal and cross-sectional planes of maximum penetration are presented in Figs. 6 and 7 respectively. It is apparent from Fig. 5 that the velocity components in the vertical direction are much weaker than those in the x and z directions. As a result, advection is weaker in the vertical direction than that in the$x$ and z directions and the diffusion mode of thermo-solutal transport is relatively more important in the vertical direction for both laminar and turbulent pools. This gives rise to shallower molten pools with a large width to depth ratio. The isotherms in the longitudinal directions in Fig. 6a and b clearly suggest that the thermal transport in both laminar and turbulent pools is predominantly diffusion-driven. The cross-sectional views of the thermal field (see Fig. 6c and d) also indicate predominantly diffusive transport. However, the cross-sectional view of isotherms exhibit a characteristic bending, due to the difference in thermal properties of Cu and Ni. The thermal diffusion is stronger in Cu than in case of Ni. As a result, Cu experiences a slower rate of rise of temperature than in case of Ni, as mentioned earlier. This attributes to the higher extent of penetration of the isotherms in the Ni rich side than that in the Cu rich side. This asymmetry in cross-sectional plane is found to be in good agreement with the previous experimental and computational studies [1,4,5]. Regarding the specific implications of turbulence on the overall thermal energy transport, it is observed that the maximum mean temperature in the turbulent pool is found to be smaller than the peak temperature obtained in a laminar pool, due to enhanced effective thermal diffusion associated with the turbulent transport. It can also be seen from Fig. 6 that the isotherms are more crowded in a laminar pool, as compared to a turbulent pool. This, in turn, indicates that the mean temperature gradient in a turbulent pool is smaller than that in the corresponding laminar pool, as attributed to the eddy-diffusive transport effects in the former.

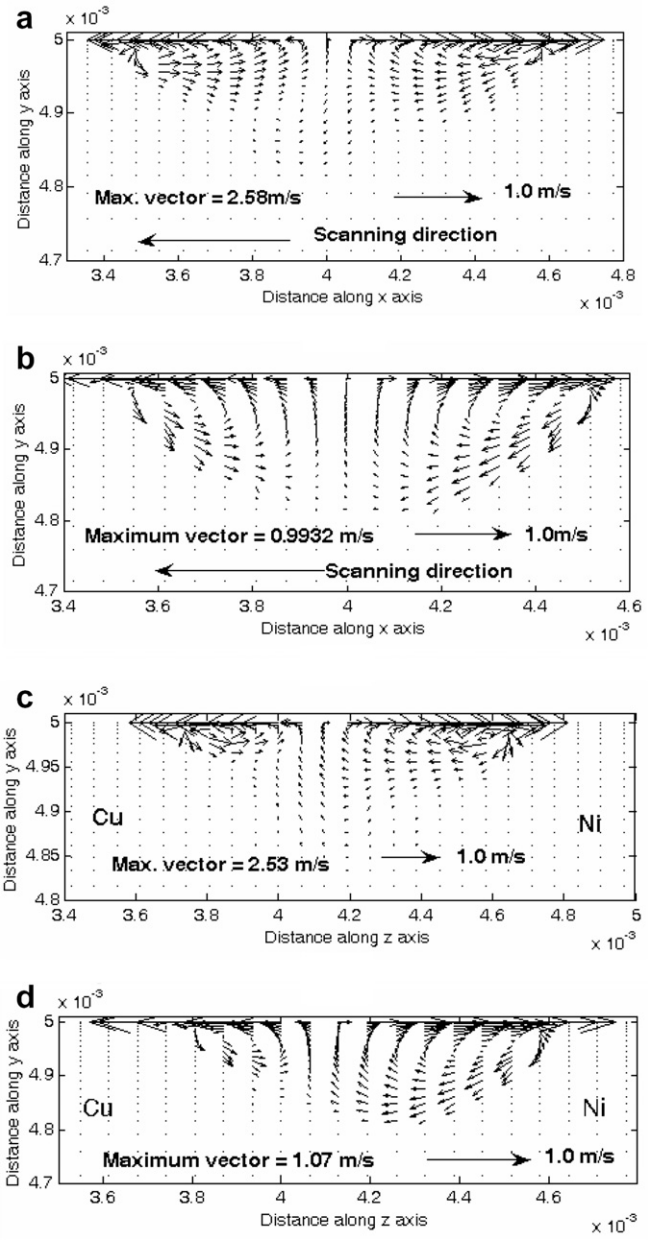

Fig. 5. Velocity vectors in the molten pool on the longitudinal plane of maximum penetration after 25 ms, for (a) laminar simulation, (b) turbulent simulation. The corresponding velocity vectors in the cross-sectional planes are shown in (c) and (d), for laminar simulation and turbulent simulation, respectively. In moving co-ordinate system laser torch located at $x = 4$ mm, $y = 5$ mm, and $z = 3.94$ mm.

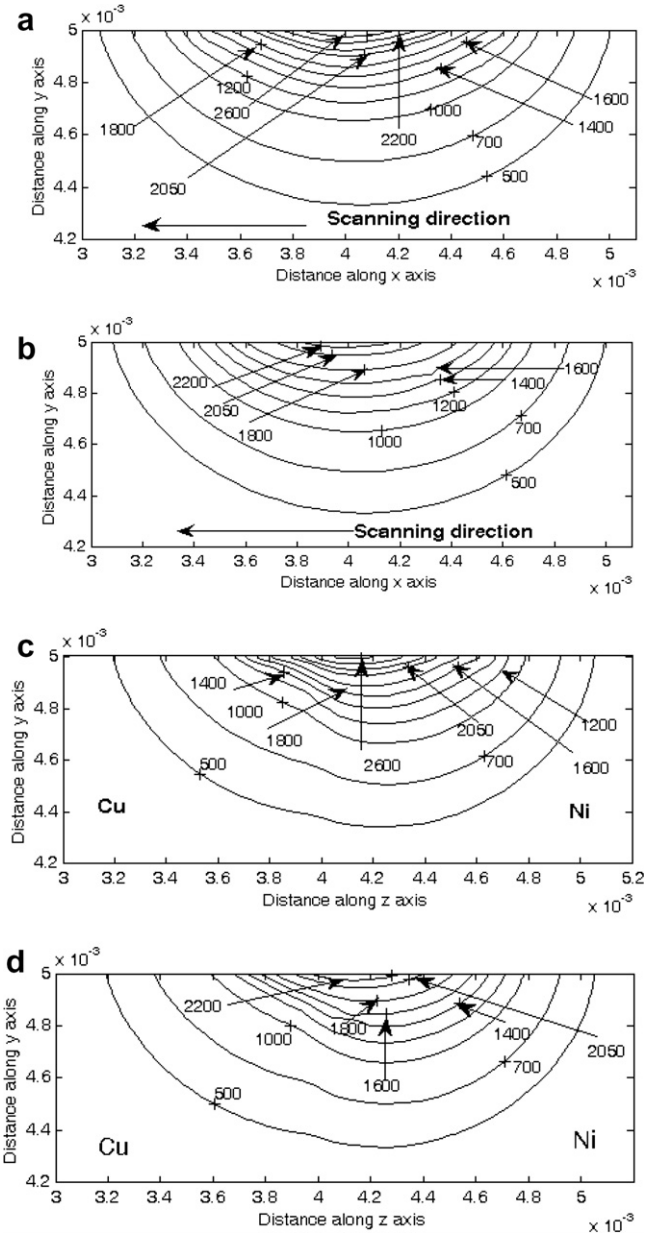

Fig. 6. Isotherms in the longitudinal plane of maximum penetration after 25 ms, for (a) laminar simulation, (b) turbulent simulation. The corresponding isotherms in the cross-sectional planes are shown in (c) and (d), for laminar simulation and turbulent simulation, respectively. In moving co-ordinate system laser torch located at $x = 4$ mm, $y = 5$ mm, and $z = 3.94$ mm. At time $t = 0$ s, $z = 3.94$ mm indicates the separation line between Cu and Ni workpieces.

The solute concentration distributions in the longitudinal and cross-sectional planes of maximum penetration for both laminar and turbulent simulation are presented in Fig. 7. It is evident from Fig. 7a and c that for laminar pool toroidal recirculation induced by Marangoni convection brings molten metals (both Cu and Ni) from the respective melting fronts and the preferentially rejected solutes from the respective solidification fronts, back to the location of the maximum temperature in the molten pool. The strength of this mean advective transport is weaker in case of turbulent transport than the advective transport in the corresponding laminar molten pool, as evident from velocity vector magnitudes in Fig. 5. However, this reduction in mean advection strength is countered by enhanced effective diffusion strength in turbulent molten pool. The resultant of these two counteracting effects eventually dictates the overall species concentration distribution in the molten pool. The Cu concentration variations in the longitudinal and cross-sectional planes, as obtained from turbulent simulation predictions, are presented in Fig. 7b

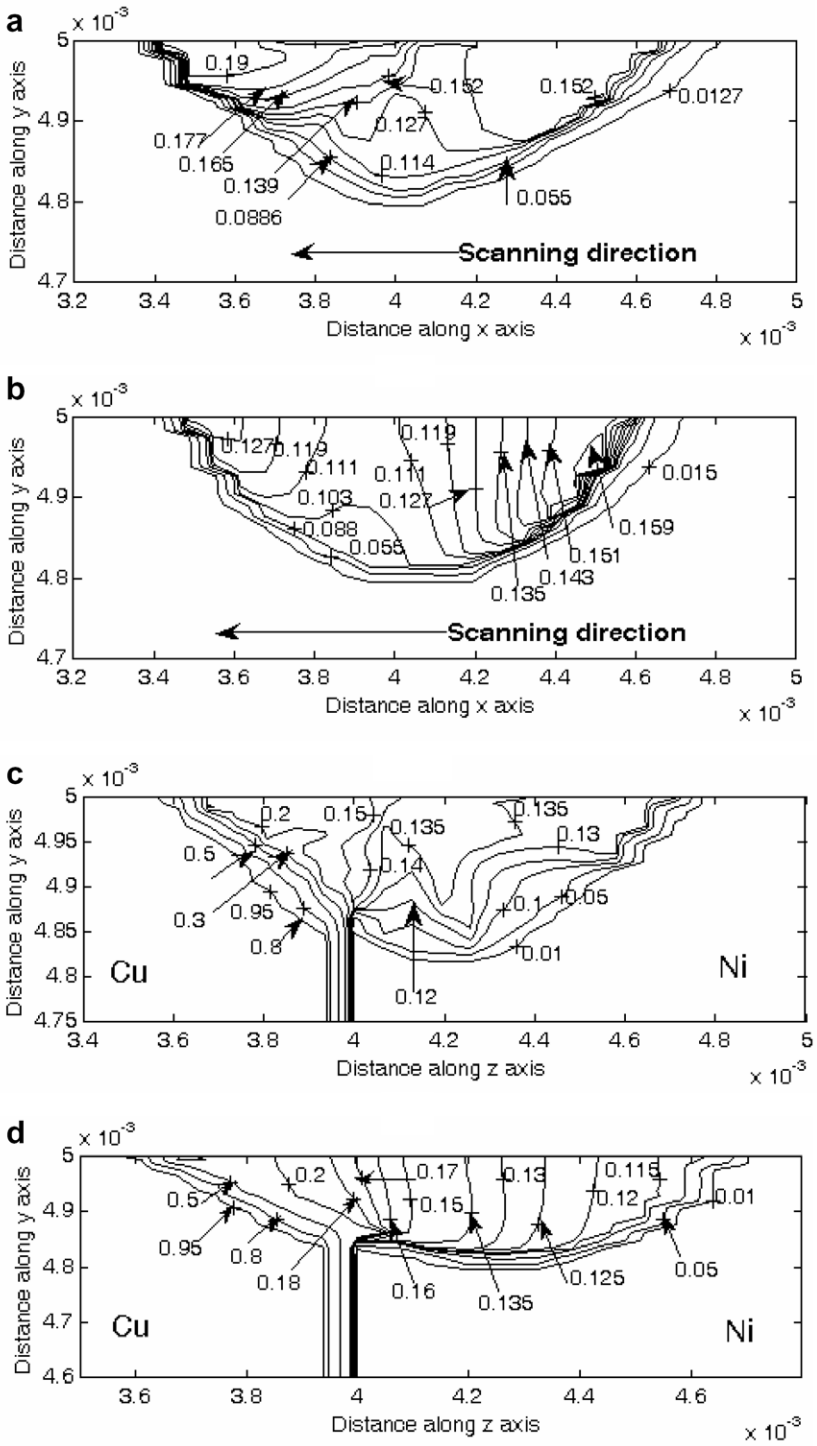

Fig. 7. Copper mass fraction contours in the longitudinal plane of maximum penetration after 25 ms, for (a) laminar simulation, (b) turbulent simulation. The corresponding contours in the cross-sectional planes are shown in (c) and (d), for laminar simulation and turbulent simulation, respectively. In moving co-ordinate system laser torch located at $x = 4$ mm, $y = 5$ mm, and $z = 3.94$ mm. At time $t = 0$ s, $z = 3.94$ mm indicates the separation line between Cu and Ni workpieces.

and d, respectively. From Fig. 7b and d, it is apparent that the concentration of Cu varies smoothly and iso-concentration contours are roughly parallel to the interface separating Cu and Ni workpieces. The nature of solutal concentration variations, as observed in Fig. 7b and d, is similar to a diffusion dominated concentration field, corresponding to a concentration gradient acting in the z direction. This clearly demonstrates that mass diffusion plays a significant role in the solutal transport, in the case of a turbulent molten pool. By contrast, in laminar molten

pool, advection is primarily responsible for solutal transport. As a result, solute transport from the solid–liquid interface gives rise to the stretching of iso-concentration contours in the direction of local fluid flow in the laminar molten pool and the extent of this stretching changes in the vertical direction owing to the change in velocity magnitudes across the pool depth (see Fig. 7a and c). It is also evident from Fig. 7a–d that the maximum value of the solutal concentration is smaller in the turbulent pool than that in the corresponding laminar pool, owing to the enhanced mass diffusion effects in the presence of turbulent transport.

In order to understand the factors influencing the weld pool penetration, it should first be noted that the increase in diffusion strength in turbulent pool enhances the thermal energy transport in the vertical direction, whereas the augmented momentum diffusion results in a weaker advective transport, as compared to that observed in a laminar pool. The enhancement in diffusive transport tends to increase the pool depth, whereas the weakening of advective transport in the vertical direction tends to reduce the pool penetration. The relative strength of these two competing mechanisms ultimately determines the pool depth in case of turbulent transport. Fig. 7a–d indicate that the maximum pool penetration for both laminar and turbulent pools are comparable. However, the relative variation of pool depth along the longitudinal and cross-sectional directions is smaller in turbulent pool than that in the case of a laminar pool. This indicates that the mean pool penetration obtained from the turbulent simulations is greater than that obtained from laminar simulation predictions.

In order to assess the quantitative predictive capabilities of the turbulence model developed in this study, the variation of Ni mass fraction distribution along the side-wise direction across the weld pool (i.e., z direction) obtained from laminar and turbulent simulations are compared with the experimental results reported by Phanikumar et al. [5] for the same laser power and torch scanning speed in Fig. 8. In the case of a laminar transport, Cu is advected over comparatively larger distances in the molten pool, which effectively decreases the local mass fractions of Ni. This effect is much weaker in the case of a turbulent transport, due to enhanced mixing effects and a consequent reduction in the mean advection strength. This, in turn, is consistent with higher mean Cu concentrations in a laminar pool than those in the corresponding turbulent pool, as observed in Figs. 4a–c and 7a–d. It is also worth noticing that the concentration profile obtained from a laminar simulation is found to be steeper than that obtained from a turbulent simulation. This can be attributed to weaker solutal concentration gradients prevailing in the turbulent pool, because of an enhanced diffusive mixing. It is clearly evident that although both laminar and turbulent simulations capture the qualitative variation of Ni mass fraction in a physically consistent manner, the concentration profile obtained from turbulent simulation prediction provides more accurate quantitative agreement with the corresponding concentration profile obtained from experiment [5].

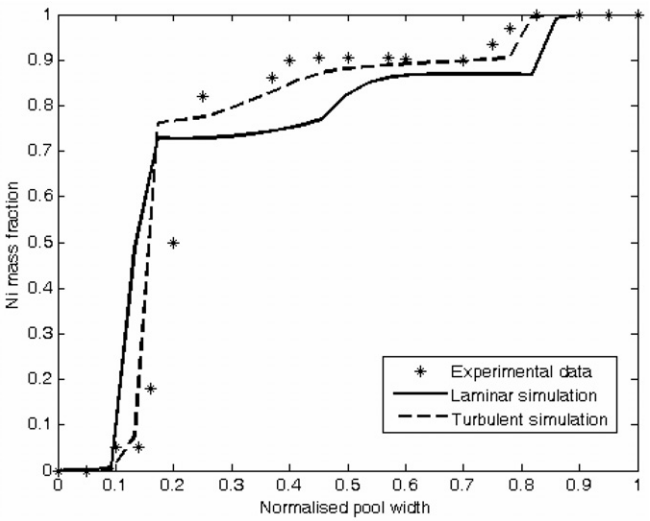

Fig. 8. Comparison between laminar and turbulent simulation predictions and the corresponding experimental results [5], for Ni mass fraction distribution along the width of the weld pool (distances are normalized with respect to the pool width).

Distributions of the turbulent kinetic energy, k, on the top surface and in the longitudinal and cross-sectional planes of maximum penetration are presented in Fig. 9. The corresponding distributions of dissipation rates of turbulent kinetic energy, ε, are depicted in Fig. 10. It is evident from Fig. 9a and c that the maximum value of turbulent kinetic energy is attained near the pool boundary in the side-wise direction. Even along the longitudinal direction, the maximum value of k is attained near the pool boundaries (see Fig. 9b). In order to analyze this behaviour, it is instructive to look to the expression of the turbulent kinetic energy generation per unit mass, P, in the context of a k–ε model, as

$$P = -\overline{u_i' u_j'}\left(\frac{\partial \bar{u}_i}{\partial x_j}\right) = C_\mu \frac{k^2}{\varepsilon}\left(\frac{\partial \bar{u}_i}{\partial x_j} + \frac{\partial \bar{u}_j}{\partial x_i}\right)\left(\frac{\partial \bar{u}_i}{\partial x_j}\right) \sim C_\mu \frac{k^2}{\varepsilon} S_t^2 \tag{36}$$

In expression (36), the mean velocity gradients are scaled as $S_t \sim U_s/l_{ref}$, where U_s is a surface velocity scale and l_{ref} is a reference length scale in the molten pool. The value of S_t is predominantly governed by velocity gradients in the y direction (i.e., $\partial \bar{u}_1/\partial x_2$ and $\partial \bar{u}_3/\partial x_2$). Accordingly, strong velocity gradients near the pool boundaries give rise to high values of turbulent kinetic energy generation in the vicinity. In the quasi-steady state, a local equilibrium is maintained between P and ε. As a result, the maximum value of ε is also attained near the pool boundaries, as evident from Fig. 10a–c. Further, scaling arguments under the equilibrium between P and ε suggest that

$$\varepsilon \sim C_\mu (k^2/\varepsilon) S_t^2 \tag{37a}$$

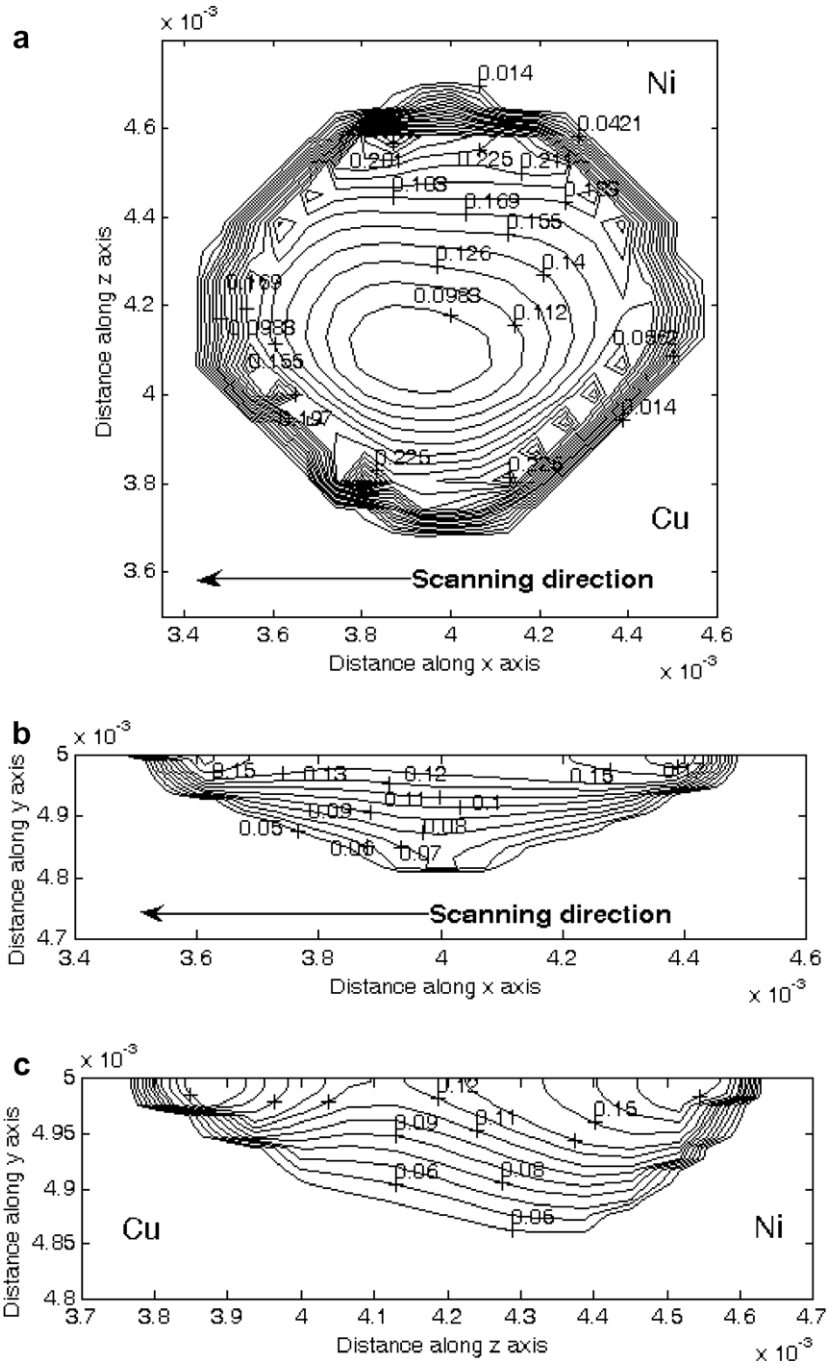

Fig. 9. Turbulent kinetic energy distribution in the molten pool after 25 ms: (a) top surface, (b) longitudinal plane with maximum penetration, (c) cross-sectional plane with maximum penetration. Contour labels are given in m^2/s^2. In moving co-ordinate system laser torch located at $x = 4$ mm, $y = 5$ mm, and $z = 3.94$ mm. At time $t = 0$ s, $z = 3.94$ mm indicates the separation line between Cu and Ni workpieces.

which leads to

$$3/2C_{\mu}^{1/2}S_{\mathrm{t}} \sim u'/l_{\mathrm{ref}} \tag{37b}$$

The above expressions are subject to the following scaling estimates: $k = 3/2u'^2$ and $\varepsilon \sim u'^3/l_{\mathrm{ref}}$, where u' is the r.m.s. of the turbulent velocity fluctuations. Since $S_{\mathrm{t}} \sim U_{\mathrm{s}}/l_{\mathrm{ref}}$, expression (37b) suggests that

$$u' \sim 3/2\sqrt{C_{\mu}}U_{\mathrm{s}} \tag{38}$$

For a surface velocity scale of 1.0 m/s, expression (37) predicts u' to be in the tune of 0.45 m/s, which predicts k to be in the order of 0.10 m^2/s^2. If reference length scale, l_{ref}, is taken as $l_{\mathrm{ref}} \sim \kappa d$, where κ is the von-Karman's constant (=0.41) and d is the weld pool depth ($d \sim 10^{-4}$ m), the ε scale is found to be of the order of 100 m^2/s^3. These scaling

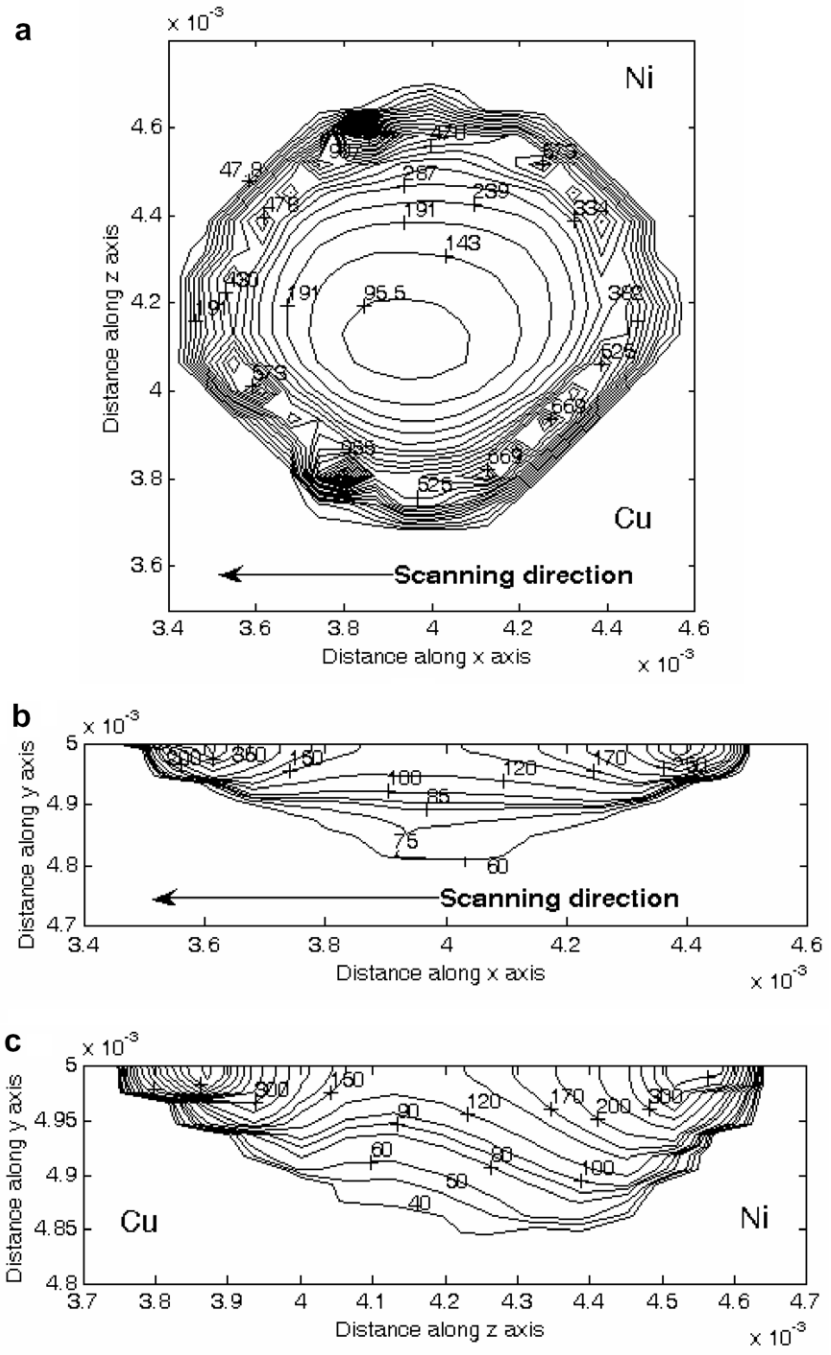

Fig. 10. Turbulent kinetic energy dissipation rate distribution in the molten pool after 25 ms: (a) top surface, (b) longitudinal plane with maximum penetration, (c) cross-sectional plane with maximum penetration. Contour labels are given in m^2/s^3. In moving co-ordinate system laser torch located at $x = 4$ mm, $y = 5$ mm, and $z = 3.94$ mm. At time $t = 0$ s, $z = 3.94$ mm indicates the separation line between Cu and Ni workpieces.

estimations are observed to be in good agreement with the order of magnitude of the corresponding simulation predictions depicted in Figs. 9a and 10a. The variation of eddy kinematic viscosity $\nu_t = \mu_t/\rho$ in the molten pool is presented in Fig. 11. It can be seen that the maximum value of ν_t is two orders of magnitude greater than the molecular kinematic viscosity of the constituent metals ($\mu_{Cu}/\rho_{Cu} = 3.2 \times 10^{-7}\ m^2/s$ and $\mu_{Ni}/\rho_{Ni} = 4.65 \times 10^{-7}\ m^2/s$). The distribution pattern of ν_t in the molten pool is determined by relative magnitudes of k and ε. Fig. 11a and c clearly indicate that the maximum value of ν_t is attained on the Ni side of the molten pool, due to high values of k and moderate values of ε towards the Ni side of the molten pool, as observed in Figs. 10a–c and 11a–c. The high values of ν_t on the Ni side enable a stronger diffusion of freshly added Ni from the melting front towards the centre of the molten pool, as noted earlier in the context of Fig. 3.

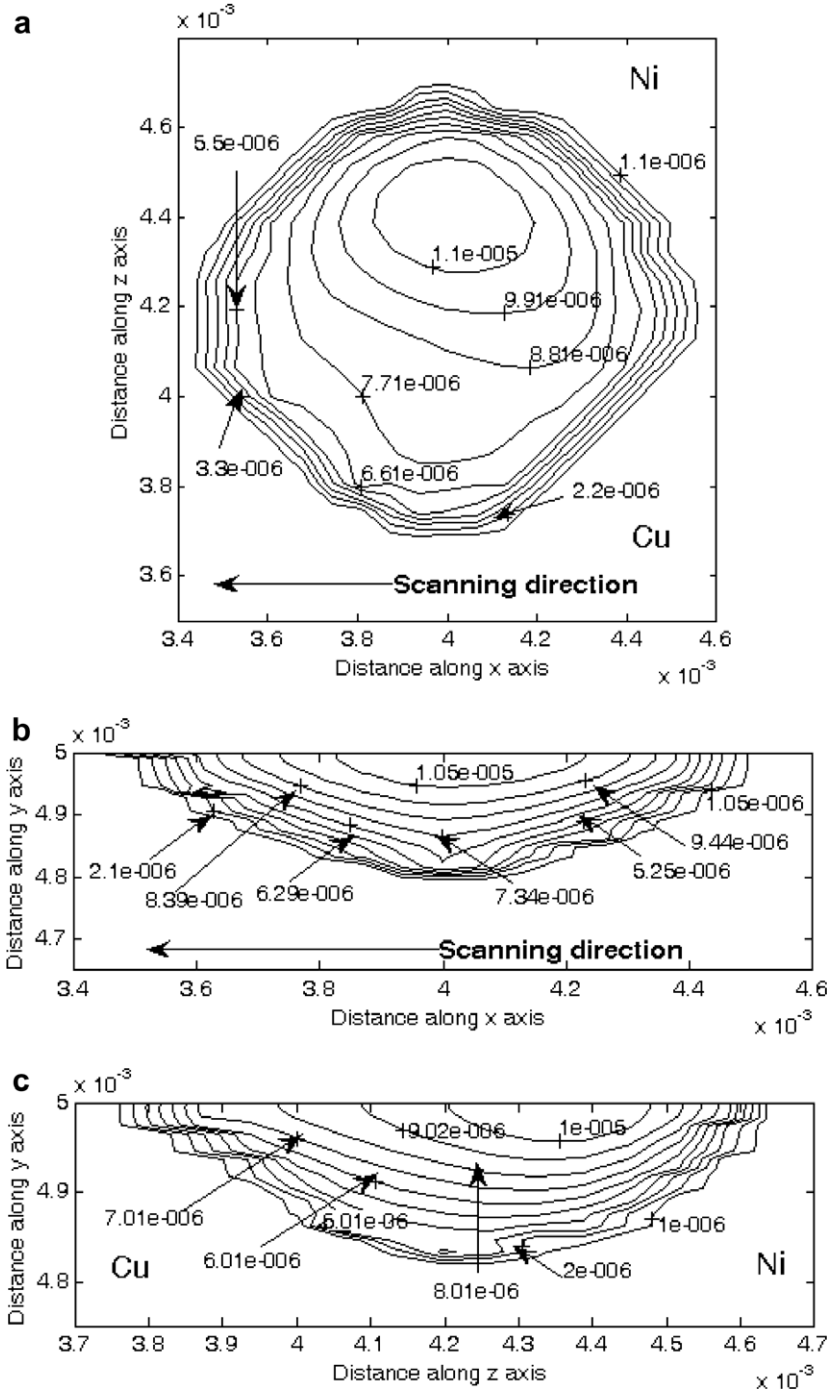

Fig. 11. Eddy kinematic viscosity μ_t/ρ distribution in the molten pool after 25 ms: (a) top surface, (b) longitudinal plane with maximum penetration, (c) cross-sectional plane with maximum penetration. Contour labels are given in m^2/s. In moving co-ordinate system laser torch located at $x = 4$ mm, $y = 5$ mm, and $z = 3.94$ mm. At time $t = 0$ s, $z = 3.94$ mm indicates the separation line between Cu and Ni workpieces.

5. Conclusions

In the present study, two sets of three-dimensional simulations are carried out for analysing the effects of turbulence on the transport characteristics associated with typical laser welding processes of Cu–Ni dissimilar couples. In one set of the simulations, the turbulent convection is accounted for by a suitably modified k–ε model, whereas the turbulence model is deactivated for the other set of simulations. The simulation parameters are chosen in such a manner that the effects of turbulent convection can be prominently manifested in the molten pool transport. It is observed that the thermo-solutal transport phenomena are significantly affected by turbulence in the molten pool. The gradients in velocity, temperature and concentration are found to be smaller in the turbulent molten pool than

the corresponding values obtained from laminar simulation because of enhanced mixing effects associated with eddy-diffusive transport. In addition to that, the maximum values of these quantities are also found to be smaller in the turbulent pool than the corresponding magnitudes obtained from the laminar simulation. In particular, the effects of turbulence are observed to be most prominent in the case of solutal transport, since the eddy mass diffusivities turn out to be several orders of magnitude higher than the corresponding molecular mass diffusion coefficients of molten metals. The solutal concentration distribution, as obtained from the turbulent simulation, is also found to be in a better agreement with the corresponding experimental results in comparison to the laminar transport model based predictions.

Acknowledgements

The authors gratefully acknowledge the useful discussions with Dr. G. Phanikumar of the Indian Institute of Technology, Madras.

References

[1] F.F. Chung, P.S. Wei, Mass, momentum and energy transport in molten pool when welding dissimilar metals, J. Heat Transfer 121 (1999) 451–461.
[2] P.S. Wei, F.K. Chung, Unsteady Marangoni flow in a molten pool when welding dissimilar metals, Metall. Mater. Trans. B 31B (2000) 1387–1403.
[3] P.S. Wei, Y.K. Kuo, J.S. Ku, Fusion zone shapes in electron-beam welding dissimilar metals, Trans. ASME, J. Heat Transfer 122 (2000) 626–631.
[4] G. Phanikumar, P. Dutta, K. Chattopadhyay, Modelling of transport phenomena in laser welding of dissimilar metals, Int. J. Numer. Methods Heat Fluid Flow 11 (2001) 156–171.
[5] G. Phanikumar, P. Dutta, K. Chattopadhyay, Computational modelling of laser welding of Cu–Ni dissimilar couple, Met. Trans. B 35B (2004) 339–350.
[6] D.R. Atthey, A mathematical model for fluid flow in a weld pool at high currents, J. Fluid Mech. 98 (1980) 787–801.
[7] M. Aboutalebi, R.M. Hassan, R.I.L. Guthrie, Numerical study of coupled turbulent flow and solidification for steel slab clusters, Numer. Heat Transfer, Part A 28 (1995) 279–299.
[8] W. Shyy, Y. Pang, G. Hunter, B.D.Y. Wei, M.H. Chen, Modelling of turbulent transport and solidification during continuous ingot casting, Int. J. Heat Mass Transfer 15 (1992) 1229–1245.
[9] A. Bejan, Convection Heat Transfer, 2nd ed., John Wiley and Sons, 1995.
[10] Y. Joshi, P. Dutta, D. Espinosa, P. Schupp, Non-axisymmetric convection in stationary gas tungsten arc weld pools, Trans. ASME, J. Heat Transfer 119 (1997) 164–171.
[11] K. Mundra, T. Debroy, T. Zacharia, S. David, Role of thermophysical properties in weld pool modeling, Weld. J. 71 (1992) 313–320.
[12] R.T.C. Choo, J. Szekely, The possible role of turbulence in GTA weld pool behaviour, Weld. J. 73 (1994) 25–31.
[13] K. Hong, D.C. Wakeman, A.B. Strong, The predicted influence of turbulence in stationary gas tungsten arc welds, in: Trends in Welding Research, Proceedings of 4th International Conference, Gatinberg, Tennessee, 1995, pp. 399–404.
[14] N. Chakraborty, S. Chakraborty, P. Dutta, Modelling of turbulent transport in arc welding pools, Int. J. Numer. Methods Heat Fluid Flow 13 (2003) 7–30.
[15] N. Chakraborty, S. Chakraborty, P. Dutta, Three dimensional modelling of turbulent weld pool convection in GTAW process, Numer. Heat Transfer A 45 (2004) 391–413.
[16] N. Chakraborty, S. Chakraborty, Influences of positive and negative surface tension coefficients on laminar and turbulent weld pool convection in a gas tungsten arc welding (GTAW) process: a comparative study, Trans. ASME, J. Heat Transfer 127 (2005) 848–862.
[17] N. Chakraborty, D. Chatterjee, S. Chakraborty, Modelling of turbulent transport in laser surface alloying, Numer. Heat Transfer A 46 (2004) 1009–1032.
[18] N. Chakraborty, D. Chatterjee, S. Chakraborty, A scaling analysis of turbulent transport in a laser surface alloying process, J. Appl. Phys. 96 (2004) 4569–4577.
[19] P. Dutta, Y. Joshi, C. Frenche, Determination of gas tungsten arc welding efficiencies, Exp. Thermal Fluid Sci. 9 (1994) 80–89.
[20] M.B. Carver, Numerical computation of phase separation in two fluid flow, J. Fluids Eng. 106 (1984) 147–153.
[21] M. Ishii, K. Mishima, Two-fluid model and hydrodynamic constitutive relations, Nucl. Eng. Des. 82 (1984) 107–126.
[22] A.D. Brent, V.R. Voller, K.J. Reid, Enthalpy-porosity technique for modelling convection–diffusion phase change: application to the melting of a pure metal, Numer. Heat Transfer 13 (1988) 297–318.
[23] P. Durbin, B.A. Petterson Reif, Statistical Theory and Modelling for Turbulent Flows, 1st ed., John Wiley & Sons Ltd., 2001.
[24] M.C. Flemmings, Solidification Processing, McGraw-Hill, New York, 1974.
[25] B.A. Kader, Temperature and concentration profiles in fully turbulent boundary layers, Int. J. Heat Mass Transfer 24 (1981) 1541–1544.
[26] S.V. Patankar, Numerical Heat Transfer and Fluid Flow, Hemisphere, Washington, DC, 1980.
[27] F.A. Brandes, Smithells Metals Reference Book, 6th ed., Butterworths & Co. Publications, London, 1983.
[28] S. Chakraborty, S. Sarkar, P. Dutta, Scaling analysis of momentum and heat transport in gas tungsten arc welding pools, Sci. Technol. Weld. Join. 7 (2) (2002) 88–94.